IAC-18-B4.6B.3

Flight Results of the Mission of TNS-0 #2 Nanosatellite Connected via Global Communication System

Mikhail Ovchinnikov [a], Danil Ivanov[b]*, Oleg Pansyrnyi [c], Igor Fedorov [d], Arnold Selivanov [e], Oleg Khromov [f], Nikolay Yudanov [g], Artem Sergeev [h]

[a] *Keldysh Institute of Applied Mathematics, RAS, Miusskaya sq.4, Moscow, Russian Federation, 125047,* ovchinni@keldysh.ru
[b] *Keldysh Institute of Applied Mathematics, RAS, Miusskaya sq.4, Moscow, Russian Federation, 125047,* danilivanovs@gmail.com
[c] *JSC Russian Space Systems, Aviamotornaya st. 53, Moscow, Russian Federation, 111250,* pantsyrnyi@mail.ru
[d] *JSC Russian Space Systems, Aviamotornaya st. 53, Moscow, Russian Federation, 111250,* tm016@rniikp.ru
[e] *JSC Russian Space Systems, Aviamotornaya st. 53, Moscow, Russian Federation, 111250,* selivanov@rniikp.ru
[f] *JSC Russian Space Systems, Aviamotornaya st. 53, Moscow, Russian Federation, 111250,* khromovoe@mail.ru
[g] *JSC Russian Space Systems, Aviamotornaya st. 53, Moscow, Russian Federation, 111250,* kolyan2606@mail.ru
[h] *JSC Russian Space Systems, Aviamotornaya st. 53, Moscow, Russian Federation, 111250,* vorchun@yandex.ru
* Corresponding Author

Abstract

The flight results of the Technological NanoSatellite TNS-0 #2 is presented in the paper. The main feature of the TNS-0 nanosatellite series is to use the Globalstar communication system. The details on the communication sessions are given in the paper. The main purpose of the nanosatellite TNS-0 № 2 is to obtain the flight qualification of the instruments and sensors installed onboard. The results of the attitude motion determination using magnetometer and sun sensors data during the mission are presented in the paper. Using the measurements of GPS/GLONASS receiver the TNS-0 #2 orbit degradation in the dense layers of the atmosphere is tracked.
Keywords: nanosatellite, attitude determination, global communication system

1. Introduction

Technological NanoSatellite TNS-0 #2 developed by JSC Russian Space Systems was successfully launched on August 17, 2017 from the International Space Station during the spacewalk of the Russian cosmonauts. The mass of the satellite is 4.8 kg and the form-factor is hexagonal prism. The main feature of the TNS-0 nanosatellite series is to use the Globalstar communication system. The TNS-0 satellites upload and download the telemetry and other information via Globalstar antennas installed onboard. For successful communication session it is necessary the TNS-0 and Globalstar satellites are to be in the line of sight, and at the same time the Globalstar satellite and the ground receiving station are also to be in the line of sight. Such a situation for the TNS-0 #2 occurs about 15 times in a day and the communication intervals vary from one up to three minutes.

The main purpose of the nanosatellite TNS-0 № 2 is to obtain the flight qualification of the instruments and sensors installed onboard. It is equipped with the passive magnetic attitude system developed by the Keldysh Institute of Applied Mechanics RAS. The system consists of a set of hysteresis rods for initial angular velocity damping and a permanent magnet located along the axis of symmetry to stabilize the axis along the local geomagnetic field induction vector. Three-axis magnetometer, a set of photodiode sun sensors, a single ultraviolet one and an infrared horizon sensor are installed onboard.

Passive magnetic attitude control systems were widespread at the dawn of the space age. A number of papers on attitude dynamics of satellites equipped with magnetic dampers and permanents magnets are well-known [1–5]. However, these attitude systems have become popular again with the advent of small and nano-satellites due to strict limitations in terms of mass, size, cost and energy on these satellites. One can mention nanosatellites Munin (2000г.) [6], QuakeSat (2003г.) [7], CUTE-I XI-IV (2003г.) [8], EduSAT (2011 г.) [9], Delfi-C3 (2008г.) [10]. Particular interest in the development and use of passive attitude magnetic systems is shown by universities and small companies entering the market of space services.

The algorithms of attitude motion determination using on-board sensors measurements are well studied in the literature. There are two main approaches the real-time on-board motion estimation using recursive algorithms [11,12] and post-flight measurement processing for motion reconstruction. The first approach is commonly used for active attitude control systems, and the second is more suitable for motion estimation of satellites with passive attitude control systems. In this paper magnetometer measurements processing technique is used for TNS-0 #2 nanosatellite attitude motion reconstruction. The technique is similar to the one that used for motion determination of Photon and

Bion series satellites [13–15]. It consists in finding such initial conditions for the equations of angular motion at which the minimum of the difference of the squares of magnetic field measurements and predicted measurements calculated using the model of the angular motion of the satellite is reached.

The structure of the paper is as follows. In the first section, the TNS-0 #2 satellite and its systems are described, the main parameters of its elements are listed, their choice is justified, and the position of the sensors in the satellite body is presented. In the second section, a technique is presented for processing the measurements of the Earth's magnetic field using a magnetometer and solar sensors measurements. The third section presents the results of applying this technique to determine the angular motion of the satellite after launch from the International Space Station, the time of transient processes is found, and the accuracy of magnetic stabilization is estimated. In the fourth section an information about obtained during the year communication sessions using Globalstar antenna. The degradation of the orbit altitude using TLE and GPS/GLONASS-receiver is presented.

2. TNS-0 #2 description

TNS-0 #2 nanosatellite has a body in the shape of hexagonal prism with 26.4 cm height and 18.7 cm of diameter. The sides of the device are covered with solar panels. Globalstar antennas, a set of solar sensors and a radio link antenna are located on the upper side of the satellite. A handle is attached to the bottom of the prism, for which the astronaut keeps the satellite on launch during the spacewalk. The satellite is presented in Fig. 1.

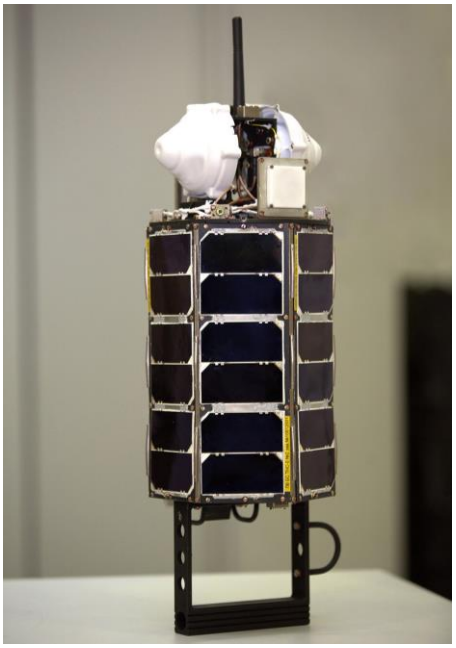

Fig. 1. The photo of the TNS-0 #2 nanosatellite

The mass of satellite is 4.8 kg, its center of mass is located on the axis of geometric symmetry of the satellite body, as shown in Fig. 2. The elements of the inertia tensor in the reference frame located in the center of mass of the satellite have the following values:

$$J = \begin{bmatrix} 0.06153 & -0.00013 & -0.00033 \\ -0.00013 & 0.06669 & -0.00012 \\ -0.00033 & -0.00012 & 0.01287 \end{bmatrix} \text{kg} \cdot \text{m}^2.$$

The value of the permanent magnet is equals to 2.2 $\text{A}\cdot\text{m}^2$. A grid of hysteresis rods is installed on the upper and lower sides of the nanosatellite body, they are used for damping the angular velocity after the launch. The location of the permanent magnet, as well as the magnetometer and solar sensors on the body of the satellite is shown in Fig. 2.

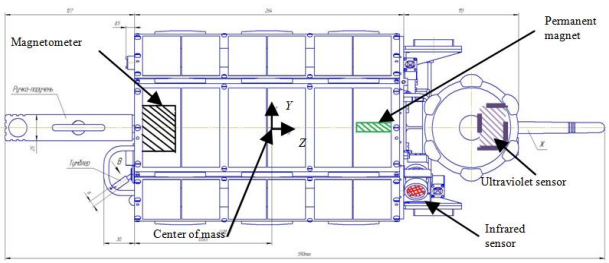

Fig.2. Center of mass location, permanent magnet, magnetometer and sun sensors position in the satellite body

2.1 Permanent magnet

A passive magnetic attitude system is installed on TNS-0 #2 nanosatellite to ensure the restoring and damping torques. The restoring torque is implemented by means of a permanent magnet. A damping system consisting of hysteresis rods of a soft magnetic material is chosen to solve the problem of dissipating the energy of the disturbed attitude motion.

A permanent magnet must provide such a restoring torque to dominate in comparison with the gravitational and aerodynamic torques. Besides, the value of the dipole magnetic moment should not fall in the region of external and parametric resonances. External resonances are due to the proximity of the natural frequencies of the satellite attitude motion to the frequencies of the change in the forced torque. Parametric resonance is caused by a periodic change in the natural frequency of the oscillations due to a systematic change in the magnitude of the vector **B** during the satellite motion along the orbit.

A characteristic parameter that determines the amplitude of the constrained oscillation and frequency of the satellite's natural oscillations relative to the vector **B** is a dimensionless magnetic parameter η, which is defined as the ratio of the characteristic value of the restoring magnetic torque mB_0 to the value $A\omega_0^2$:

$$\eta = \frac{mB_0}{A\omega_0^2}.$$

Here m is a value of the dipole moment vector of a permanent magnet, B_0 is a magnitude of the geomagnetic field induction vector at the equator, A is equatorial moment of inertia of the satellite, ω_0 is an orbital angular velocity of the satellite. The study of the dependence of the constrained periodic oscillations amplitude on the parameter η and the dynamics analysis of the satellite with passive and active magnetic attitude systems are presented in [16]. The ramification curve in the (η, i) plane using the asymptotical formulae from [17] is presented in Fig. 3.

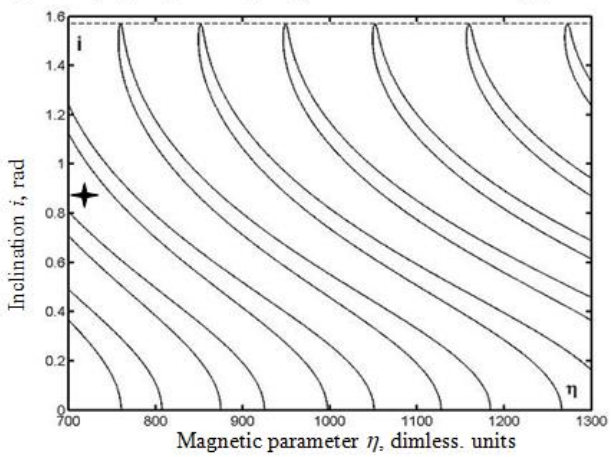

Fig. 3. Ramification curves in the vicinity of η=1000 and the value for the TNS-0 #2

A permanent magnet is installed along the symmetry axis of the satellite (Fig. 2). Its magnetic moment is close to be co-directed with this axis. Based on the results of calculations, a magnet in the form of a cylinder 34 mm in height and a base radius of 4.5 mm was chosen, the induction of the magnet is $B = 1.3$ T. The dipole moment of the magnet is determined by the formula

$$m = \frac{VB}{\mu_0},$$

where V is the volume of the magnet, μ_0 is magnetic constant. So, the magnetic dipole moment m equals to 2.2 A·m^2. Under the values of equatorial moment of inertia $A = 6.2 \cdot 10^{-2}$ kg·m^2 and orbit altitude 420 km ($\omega_0 = 1.144 \cdot 10^{-3}$ s^{-1}, $B_0 = 2.61 \cdot 10^{-5}$ T), the magnetic parameter $\eta = 710$. Then for the ISS orbit inclination $i = 51.7^\circ$ the value of the η is between two resonance curves, as one can see from Fig.3. This allows to predict the small amplitude of the oscillations of the axis of symmetry of the satellite relative to the vector **B** during the flight.

2.2 Hysteresis rods

The efficiency of the hysteresis rods depends on many factors: their volume and elongation, the material used, the layout. By elongation of the rod is meant the ratio of its length to the diameter. It is known [18] that there is an optimal elongation, the value of which usually lies in the range of 200 to 300. Among the soft magnetic materials available on the market, one of the most effective and affordable is the alloy of molybdenum-permalloy of grade 79HM.

If the distance between parallel identical rods is more than 0.3 - 0.4 of their length, then their mutual influence can be neglected. If the rods are located closer to each other, this influence is manifested in the mutual demagnetization of the rods and, consequently, in reducing their effectiveness as a damper. At a distance of 0.02 length, two rods are equivalent to one. The rods located mutually perpendicular almost do not affect each other. To avoid the influence of a permanent magnet, hysteresis rods are located in planes perpendicular to the magnetic moment vector of the magnet. For this purpose, the rods are mounted on the upper and lower sides of the satellite body as shown in Fig. 4. The number and location of the rods are chosen based on the design possibilities and considerations of maximizing the efficiency of the rods, which is proportional to their length and inversely proportional to the distance between them.

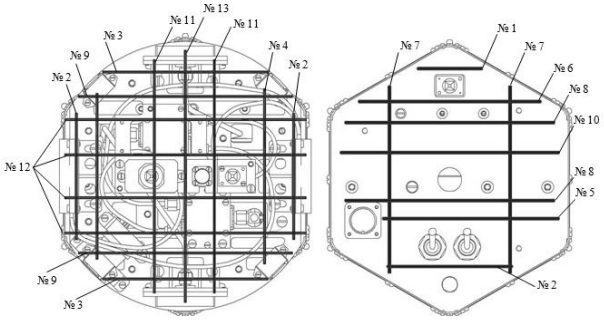

Fig. 4. Location of hysteresis rods on the bases of the THS-0 №#2 (on the left - the upper base, to the right - the bottom base)

Hysteresis rods have a square cross-section with a side of $a = 1$ mm. The satellite has 24 rods with a length from 42 mm to 164 mm. The efficiency of the rods is determined by the amount of energy dissipated during their magnetization reversal. It can be estimated from the area of the hysteresis loop in the laboratory [19]. However, due to the effect of demagnetization, the smaller the length of the rod, the smaller the area has a loop. The hysteresis losses of the rod regardless for mutual influence can be estimated as hysteresis losses per unit volume, multiplied by volume V ,

$$E_{loss} = S_{gist} \cdot V ,$$

where S_{gist} is the loop area when the rod is reversed in the geomagnetic field (geomagnetic induction near $H = 40$ A/m). The total hysteresis loss is the sum of the losses of each rod (the coercive force of the rods is assumed to be $H_e = 2$ A/m) and are equal to $E_{loss} = 1.9 \cdot 10^{-6} J$.

2.3 Magnetometer

The magnetometer installed on the satellite TNS-0 # 2 is designed for measuring the external magnetic field. The root-mean-square error of measurements of the magnetometer is $\sigma = 100$ nT. The non-orthogonality of the measuring axes is 1 degree.

Magnetometer measurements are influenced by magnetic fields created on the satellite, in particular, by the passive magnetic attitude control system. Thus, it is necessary to take into account the effect of permanent magnet fields and hysteresis rods during the processing of measurements. The magnetic field value caused by permanent magnet is less, the greater the distance from it to magnetometer. So, the magnetometer and magnet are separated as far as possible inside the satellite body to reduce the contribution from a permanent magnet in measurements. A permanent magnet is attached to the upper side of the body, and the magnetometer is mounted on the bottom base. The magnetic induction of the field of a permanent magnet is calculated as the magnetic induction of the dipole field by the formula

$$\mathbf{B} = \frac{\mu_0}{4\pi}\left(\frac{3(\mathbf{mr})}{r^5}\mathbf{r} - \frac{\mathbf{m}}{r^3}\right),$$

where **B** is vector of induction of the permanent magnet field, **m** is the vector of magnetic dipole moment, **r** is radius-vector drawn from the center of the magnet to the point at which the magnetic field is calculated, r is the magnitude of the vector.

A variable component can also be present in the magnetometer measurements in addition to constant bias. It can be caused by alternating magnetic fields as a result of turning on and off the transceivers, on-board devices, and also caused by currents in the solar panel in the sunlit part of the orbit. To study the variable on-board magnetic fields that affect the measurements of the magnetometer, in-flight instruments of the satellite were consistently switched on and off in the laboratory conditions, while the satellite itself was motionless. Measurements were obtained from an on-board magnetometer during on and off, then the satellite solar panels were successively illuminated using a Sun imitator. As a result of the tests, the measurements of the magnetometer did not deviate from a constant value by more than 200 nT. This value is negligibly small and comparable with the noise component of the measurements of the order of 100 nT. Such a low level of the alternating magnetic field is achieved, in particular, due to the special arrangement of all the supply wires on the satellite, in which the emerging magnetic field around the wires is sufficiently small.

2.4 Optical sensors

Eight optical sensors are installed on the nanosatellite THS-0 #2: six photodiode sensors, one ultraviolet solar sensor and one infrared horizon sensor. In Fig. 5 shows the placement of the optical sensors on the upper base of the satellite (the sixth photodiode solar sensor is mounted on the bottom base). The photodiode sensors No. 5 and No. 3 are coaxial with the ultraviolet and infrared sensors, respectively.

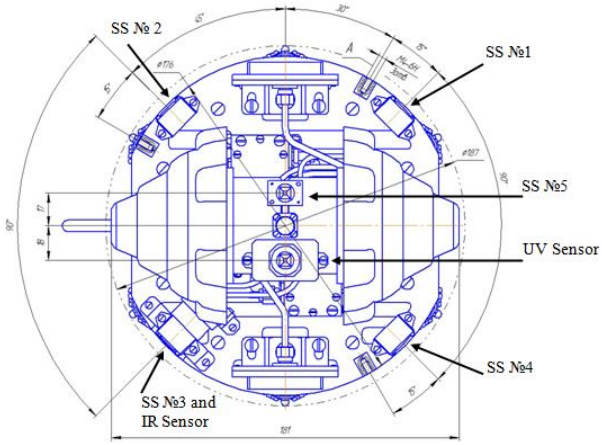

Fig. 5. Location of optical sensors THS-0 #2

Photodiode sensors measure the voltage on the photodiode sensing element, which depends on the angle between normal vector to the sensing element and Sun direction, usually according to a law close to the cosine. Thus, one can calculate the direction to the Sun in the satellite body reference frame using measurements from several photodiode sensors. However, the measurement of such sun sensors is affected by the Earth's albedo, i.e. by the light reflected from the Earth surface. The reflected light power could be up to 30% of the solar illumination power. The coefficient of reflection depends on many factors - the type of the Earth's surface from which the light reflected, clouds, time of the year. So, the creation of a sufficiently accurate model of the Earth's albedo is complicated. That is why the accuracy of the sun direction determination using photodiode sensors is usually not better than several degrees.

The ultraviolet sensor is deprived of this disadvantage. In the ultraviolet range of the light only the sun radiates, the Earth completely absorbs the ultraviolet waves. Thus, it is possible to determine the angle of incidence of the sun's rays using the ultraviolet sensor more accurately than using the photodiode sensors. Since the sensitive axes of the ultraviolet sensor

and the solar sensor coincide and are directed along the axis OZ of the TNS-0-#2, then it is possible to estimate the contribution from the albedo of the Earth in the measurements of the photodiode sun sensor by comparing the measurements obtained from both sensors.

An infrared sensor, or a horizon sensor, is sensitive to the heat emitted by both the Sun and Earth. When the axis of its sensing element is directed to the heat source, the sensor measures the voltage proportional to its power. The angular dimension of the Sun is much smaller than the angular size of the Earth from LEO. That is why the sensor is usually used to determine the moment of intersection of the sensitive axis of the Earth's horizon line, at this time the sensor measurements make a sharp jump. This information along with measurements of sun sensors could be used for ground-based reconstruction of the satellite angular motion. An important advantage of the infrared sensor in comparison with sun sensors is that it works both on the illuminated part of the orbit and on the shaded part. More details on the attitude control system can be found in [20].

3. Attitude motion reconstruction technique

In this section, a technique for processing of the measurements from on-board sensors of the nanosatellite TNS-0 #2 for the angular motion reconstruction using the telemetry data is presented. A mathematical model of the angular motion of a nanosatellite with assumptions is written in details.

3.1 TNS-0#2 attitude motion equations

Consider the motion of a satellite with hysteresis rods fixed in its body and a permanent magnet taking into account the gravitational and magnetic torques. Assume that the satellite is a solid body moving along a circular orbit around the Earth. The SGP4 model is used to describe the gravitational field of the Earth. The geomagnetic field is described by the IGRF model. The parallelogram model is used to describe the effect of the hysteresis in rods [21].

To write the equations of motion of the satellite, we introduce two reference frames which are used to write the attitude motion equations. $OX_OY_OZ_O$ is the orbital reference frame with origin placed in the satellite center of mass. Axis OZ_O is directed along the satellite radius-vector, OY_O is perpendicular to the orbital plane, axis OX_O complements these axes; OXYZ is the body-fixed reference frame, its axes are directed as shown in Fig.2.

The attitude motion is described using dynamic Euler equations and kinematic relations based on the quaternions, elements of the matrix of direction cosines or Euler angles. The satellite state vector consists of the angular velocity vector and the selected set of angular variables. The quaternion $\Lambda = (\mathbf{q}, q_0)$ is used as the angular variable. Here $\mathbf{q}$ is the vector part of the quaternion and the q_0 is the scalar part. Also the direction cosine matrix $\mathbf{A}$ and Euler angles α, β, γ (rotation sequence 2-3-1) are used for the torques model formulae and for the attitude position representation correspondingly.

The dynamic equations are as follows:

$$\mathbf{J}\dot{\boldsymbol{\Omega}} + \boldsymbol{\Omega} \times \mathbf{J}\boldsymbol{\Omega} = \mathbf{M}_{mag} + \mathbf{M}_{grav} + \mathbf{M}_{hyst},$$

where $\mathbf{J}$ is inertia tensor, $\boldsymbol{\Omega}$ is absolute angular velocity, $\mathbf{M}_{mag}, \mathbf{M}_{grav}, \mathbf{M}_{hyst}$ are magnetic torques caused by permanent magnet, gravitational torque and magnetic torque due to hysteresis rods correspondingly. The gravitational torque is

$$\mathbf{M}_{zp} = 3\omega_0^2 (\mathbf{A}\mathbf{e}_3) \times \mathbf{J}(\mathbf{A}\mathbf{e}_3),$$

where $\mathbf{e}_3 = (0,\ 0,\ 1)^T$ is local vertical vector in the orbital reference frame, $\boldsymbol{\omega}_0$ is the orbital angular velocity vector, that has the following components in the orbital reference frame $\boldsymbol{\omega}_0 = [0 \quad \omega_0 \quad 0]^T$. The magnetic torque due to permanent magnet is as follows:

$$\mathbf{M}_{mag} = \mathbf{m} \times \mathbf{B},$$

where $\mathbf{m}$ is dipole magnetic moment of the permanent magnet, $\mathbf{B}$ is the vector of the Earth magnetic field. The torque caused by the hysteresis rods is

$$\mathbf{M}_{hyst} = \mathbf{m}_{hyst} \times \mathbf{B},$$

where $\mathbf{m}_{gist}$ is the resulting dipole magnetic moment of all the rods. For the magnetic moment of one rod one can write the following:

$$\mathbf{m}_{hyst}^k = \mu_k V_k H_0 W \mathbf{e}_k / \mu_0,$$

where μ_k is the relative magnetic permeability of the k-th rod, V_k is its volume, H_0 is the mean value of the geomagnetic field induction $\mathbf{H}$ in the current point of the orbit, $W(H_\tau)$ is dimensionless function describing dependence of the induction of the rod related to H_0 according to the parallelogram, μ_0 is the magnetic constant; $H_\tau = \mathbf{H}\mathbf{e}_k$, $\mathbf{e}_k$ is the unit vector directed along the rod in the body reference frame.

Dynamic equations are supplemented by kinematic relations. The quaternion is used in the numerical simulation of the attitude motion. Its kinematic equation is as follows

$$\dot{\Lambda} = \frac{1}{2}\mathbf{C}\Lambda,$$

$$\mathbf{C} = \begin{bmatrix} 0 & \omega_3 & -\omega_2 & \omega_1 \\ -\omega_3 & 0 & \omega_1 & \omega_2 \\ \omega_2 & -\omega_1 & 0 & \omega_3 \\ -\omega_1 & -\omega_2 & -\omega_3 & 0 \end{bmatrix}.$$

Here $\boldsymbol{\omega} = [\omega_1, \omega_2, \omega_3]^T$ is angular velocity relative the orbital reference frame, that is calculated using the formula

$$\boldsymbol{\omega} = \boldsymbol{\Omega} - \mathbf{A}\boldsymbol{\omega}_0 .$$

3.2 Measurements processing technique

The problem of the attitude motion reconstruction is formulated as follows. It is necessary to obtain such initial conditions for the attitude motion equations that the difference between the predicted measurements calculated using measurement model and the actual measurements from the on-board sensor achieves a minimum by mean square criterion.

Consider an initial condition vector consisting of quaternion vector part $\mathbf{q}(t=0)$ and angular velocity vector $\boldsymbol{\omega}(t=0)$ at the initial time (the time of the first received telemetry with measurements):

$$\xi = \left[\mathbf{q}(t=0), \boldsymbol{\omega}(t=0)\right]^T .$$

If the vector ξ is defined, then one can calculate at each time t_k, when the measurements are available, the quaternion $\Lambda\left(t = t_k\right)$ obtained by the integration of the motion equations. Then one can predict the measurements for example of the magnetometer using the measurement model:

$$\tilde{\mathbf{b}}^k_{изм} = \mathbf{A}\left(\Lambda_k\right)\mathbf{b}^k_o ,$$

where the unit vector along the geomagnetic field in orbital reference frame $\mathbf{b}^k_o$ is calculated accordingly the orbital position of the satellite (obtained using either GPS/GLONASS receiver or by using TLE and SGP4 model) and geomagnetic model IGRF. Then the problem of the vector ξ determination reduces to the problem of the following function minimization

$$\Phi\left(\xi\right) = \sum_{k=1}^{N}\left(\left|\tilde{\mathbf{b}}^k_{\text{model}} - \mathbf{b}^k_{meas}\right|\right)^2 ,$$

where $\mathbf{b}^k_{изм}$ is the unit vector along the geomagnetic field calculated using measurements after excluding the constant bias. The minimization of the function $\Phi\left(\xi\right)$ is carried out using the nonlinear optimization methods.

4. Flight results and its analysis

4.1 Processing of the video of the launch from ISS

The TNS-0 #2 nanosatellite was launched on August 17, 2017 from the ISS by cosmonaut Sergei Ryazansky at 18:21 Moscow time during the spacewalk. The direction of the launch trajectory relative the ISS is shown on Fig. 6. The satellite identifier is 42914 / 1998-067ND. The video recording of the launch was carried out using a camera fixed to the cosmonaut's space suit, as well as a stationary camera installed on the Japanese module of the ISS "KIBO" (see Fig. 7).

The angular velocity of the spacecraft immediately after launch was estimated using video processing. Its components are was about 71 deg/s along the Z axis of the satellite and about 35 deg/s along the axis perpendicular to the Z axis (the satellite reference frame is shown in Fig. 2). The technique described in the work [22] was used for image processing.

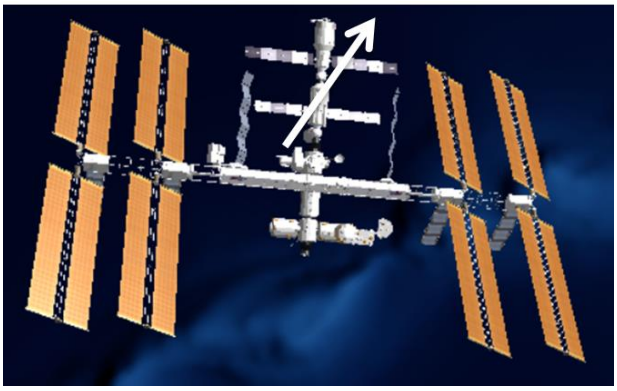

Fig. 6. The direction of the TNS-0 #2 launch from ISS

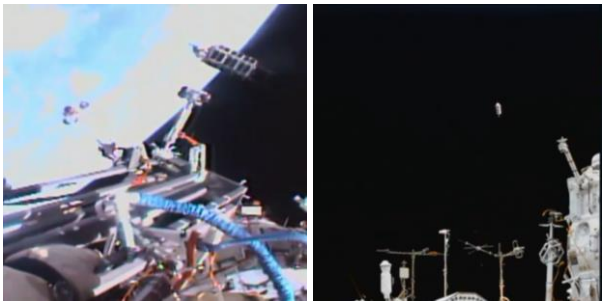

Fig. 7. Video frames of the launch obtained from the camera on the cosmonaut suit (left) and from the ISS-fixed camera (right)(3)

4.2. Attitude stabilization after the launch

The first communication session, during which the telemetry with measurements of sensors was transmitted, was on August 19 at 17 hours 11 minutes UTC. In Fig. 8 shows the graph of measurements of the magnetometer and sun sensors that lasted for one minute.

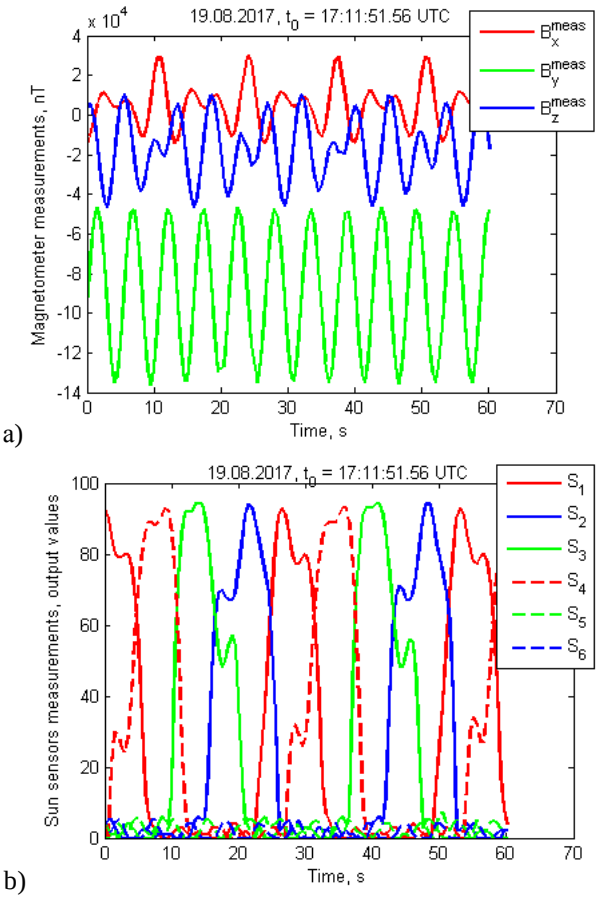

a)

b)

Fig. 8. First obtained measurements from magnetometer (a) and photodiode sensors (b)

In the measurements of the magnetometer, in addition to the geomagnetic field, there are components of constant bias due to the magnetic field of the permanent magnet (Fig. 2), as well as the variable components caused by magnetization of the hysteresis rods. To extract the measurements of the geomagnetic field, the contribution of the constant bias in the measurements was estimated using the least squares method. Fig. 9 shows a graph of the obtained Earth's magnetic field. The value of the constant bias of the magnetometer measurements is $\mathbf{B}_{bias} = [5.8 \quad -90.8 \quad -20.9] \cdot 10^3$ nT .

A unit vector along the geomagnetic field at the satellite location is calculated from the measurements obtained. Using the magnetic field model IGRF with the known position of the satellite at the time of the measurement, calculated using the TLE elements and the SGP4 motion model, a unit vector along the magnetic field in the orbital coordinate system is calculated.

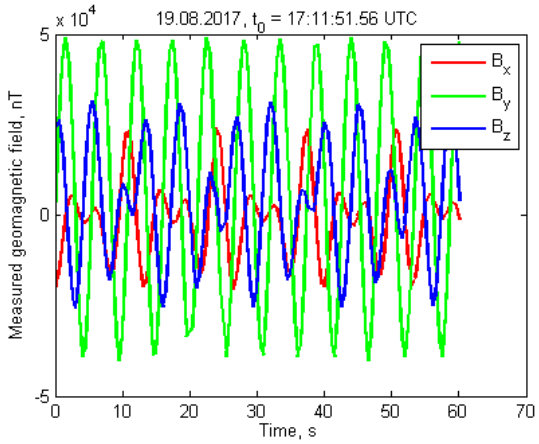

Fig.9. Measured geomagnetic field

Since the location of the magnetometer in the satellite body is known, then if one specifies the initial conditions for the angular motion, its measurement can be predicted. Thus, using the least squares method, we estimate a vector of initial conditions consisting of a quaternion and an angular velocity at the time of the measurement start, which minimizes the difference between the measured vectors along the geomagnetic field and its predicted motion model at each moment on a given telemetry segment. Fig. 10 depicts the graphs of the measured and predicted unit vector along the geomagnetic field. From this graph it can be concluded that the vector of the initial conditions close to the real one is found, since the values of the measurements and its prediction are close.

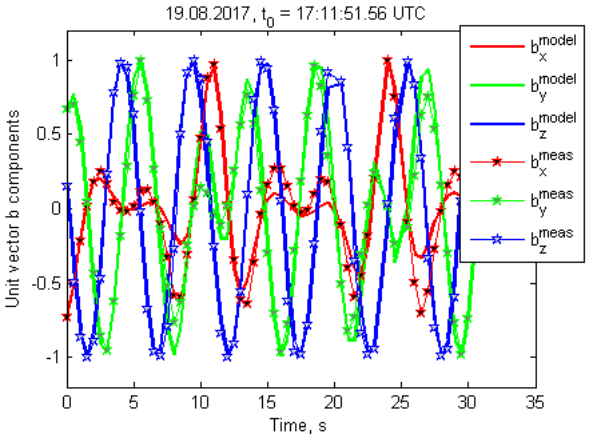

Fig. 10. Measured and predicted unit vector along the geomagnetic field

Fig. 11 shows the graphs of the quaternion and Euler angles (rotation sequence 2-3-1) calculated using the initial conditions obtained. Fig. 12 shows the angular velocity vector. Its value close to the one estimated using video of the launch processing.

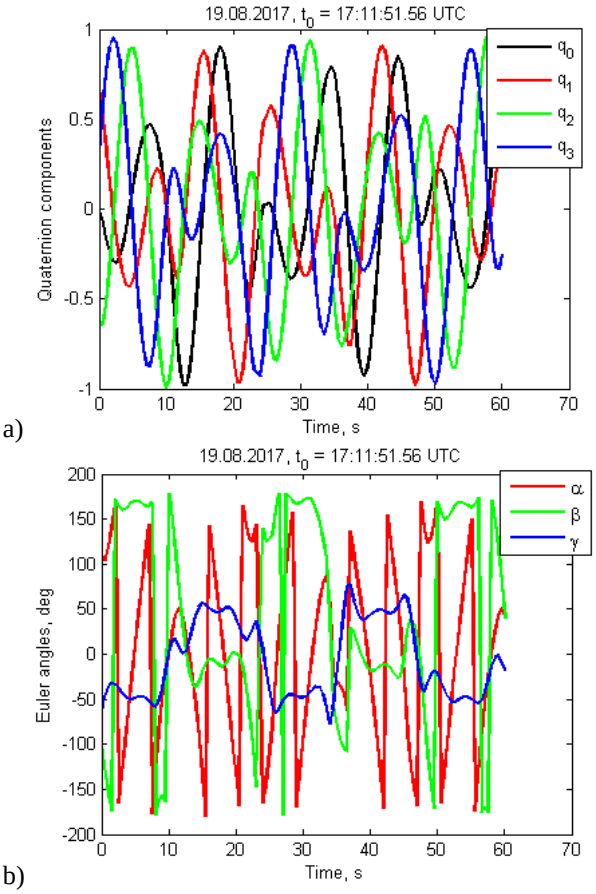

Fig. 11. Quaternion (a) and Euler angles (b)

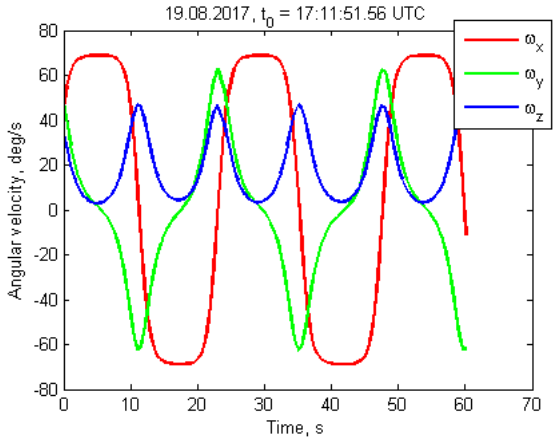

Fig.12. Angular velocity components

To verify the obtained angular motion estimation, measurements from sun sensors were predicted and a comparison with actual measurements was made. It is assumed that the photodiode sensors have a sensitive area in the form of a cone with an angle of 120 degrees. The sensor measurements within this region is considered to have a cosine-like dependence on the incidence angle of the sun's rays, and outside this region the sensors measurements are zero. The measurements of the sensors (Fig. 8b) were normalized to the maximum value according to the procedure described in the paper [20]. Fig. 13 presents a comparison of sensor measurements and its predicted values using the satellite motion model with initial conditions obtained using the magnetometer data. There is some correlation between the corresponding curves, but the discrepancy in the numerical values can be explained by the unaccounted influence of the Earth's albedo, which also affects the sun sensors measurements and its contribution can reach up to 30% of the Sun's influence. In particular, non-zero measurements from solar sensors № 5 and 6 can be explained by the effect of the light reflected from the Earth.

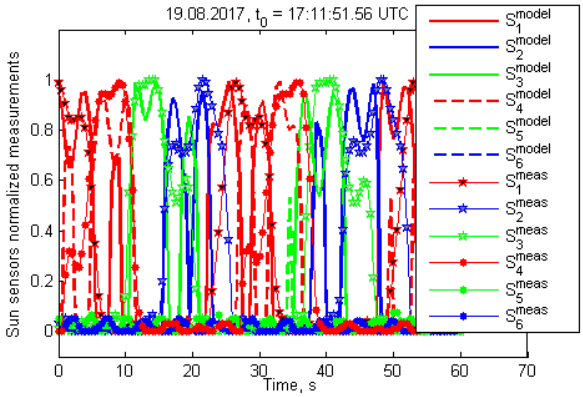

Fig. 13. Sun sensors normalized measurements and its predicted values

The measurements obtained from the telemetry was processed using the same technique. Fig. 14 shows the angular velocity graphs for telemetry segments obtained on August 24, September 4, 13 and 24 as for example. From the angular velocity graphs one can track the dynamics of the change in the angular motion of the nanosatellite. Thus, for a period of about 17 days from August 17 to September 4, the satellite changed from a rotation about all three axes (Fig. 12) to rotation predominantly relative to the Y axis (Fig.14a) This is because the moment of inertia relative to the Y axis is the largest axial moment of inertia, and the rotation relative to this axis is a stable motion. From the other graphs one can see how the angular velocity decreases due to affect of the hysteresis rods onboard.

Fig. 15 shows a graph of magnetometer measurements, from which it can be concluded that by September 24 the nanosatellite achieved the magnetic attitude, i.e. the OZ axis of the satellite tracks the direction of the induction vector of the local geomagnetic field. By the time telemetry was received, a component of angular velocity about the axis OZ remained about 1.2 deg/s (it is component relative to the magnetic field vector), and oscillations with a period of about 4 minutes and OZ axis deviation amplitude of about 15 degrees is observed.

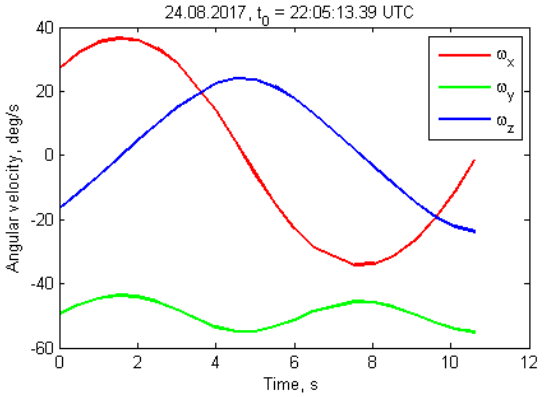

a)

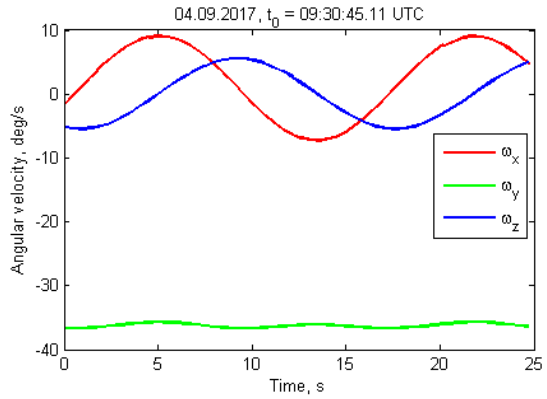

b)

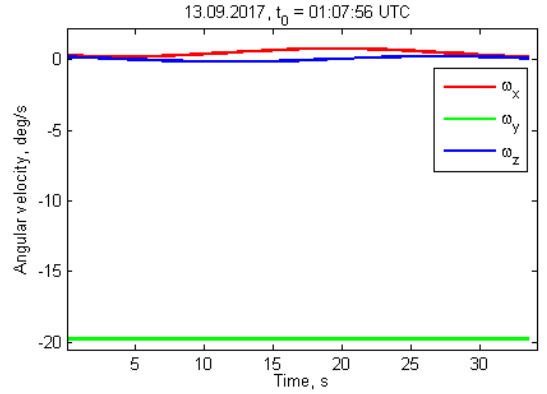

c)

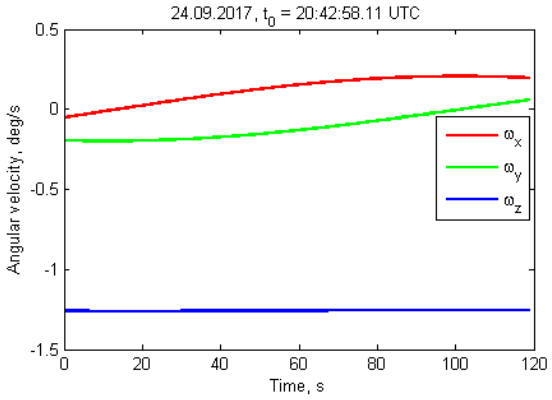

d)

Fig. 14. Angular velocity for the August 24, September 4, 13 and 24

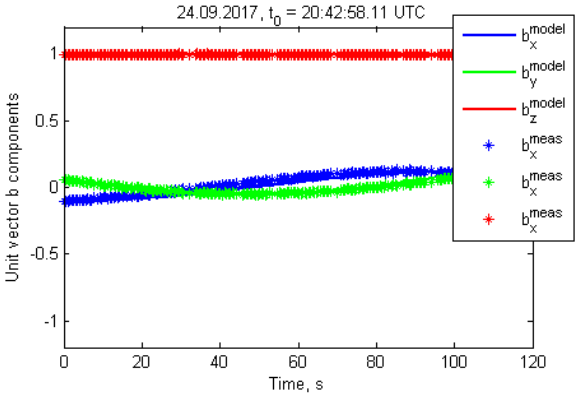

Fig. 15. Measured and predicted unit vector along the geomagnetic field

According to Fig. 12 and 14, one can trace the dynamics of the damping of the angular velocity of the THS-0 #2 satellite after the launch. Fig. 16 shows the dependence of the angular velocity modulus on time after the launch of the satellite. The graph is close to linear, which corresponds to the damping model using hysteresis dampers. From the graph it can be concluded that it took about 36 days for damping and achieving a magnetic attitude, which is due to a high initial angular velocity of 79 deg/s.

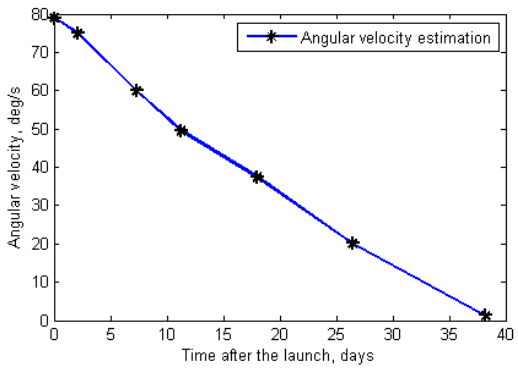

Fig. 16. Dynamics of angular velocity damping

4.3. Stabilized motion of TNS-0 # 2 nanosatellite

On October 2 it was possible to obtain telemetry recorded on the onboard storage in a time approximately equal to 2 orbits. Fig. 19 shows the measurements of the magnetometer, sun sensors, infrared horizon sensor and an ultraviolet sensors. One can see from Fig. 19b the sunlit and shadowed parts of the orbit where the photodiode sensors measurements are equal to zero. In the Fig. 19c on the shadowed part orbit infrared sensor twice was oriented towards the Earth, but on the sunlit part of the orbit the measurements are too noisy due to sun influence. The UV-sensor measurements is very smooth when the sensor axis is close to the Sun direction except two points when the sunlight was shadowed by the satellite antenna (see Fig.1).

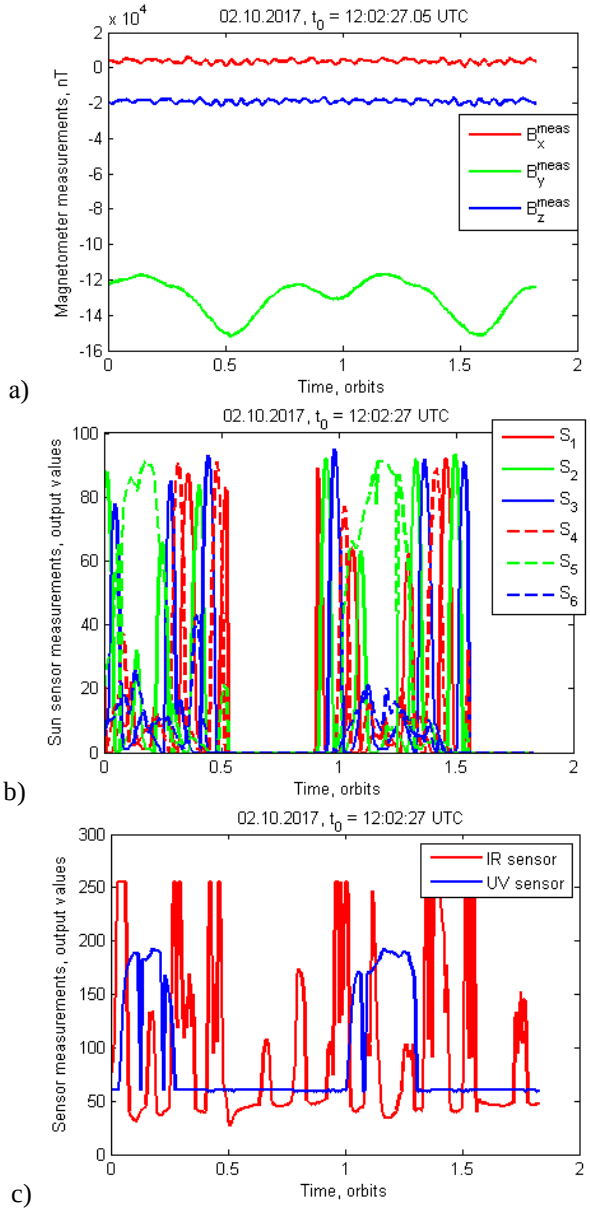

Fig. 17. Measurements of the magnetometer (a), sun sensors (b), infrared horizon sensor and an ultraviolet sensors (c)

The initial conditions for the motion model of the nanosatellite TNS-0 #2 were determined using the least squares method described above. The result is shown in Fig. 18 - comparison of magnetometer measurements and model values. Fig. 19 (a) shows a graph of the deviation angle of the OZ axis from the local magnetic field vector. It can be seen that this angle does not exceed 12 degrees, and the average deviation along the orbit is about 5 degrees. This graph can be considered almost classical. It clearly shows the characteristic period of the forced oscillations (about 9 minutes) caused by the uneven rotation of the local geomagnetic field induction vector. Its frequency is close to the frequency of the satellite's natural oscillations as a rigid body with a permanent magnet in a constant external magnetic field. The period of comparatively slow amplitude variation of these oscillations (a time equal to half the satellite's revolution in orbit around the Earth) is associated with a change in the magnitude of the induction vector of the local geomagnetic field. Fig. 19b is a graph of the angular velocity during the motion, which shows that the satellite continues to rotate about the longitudinal axis with an angular velocity of 0.4 deg/s, and two other axes oscillates.

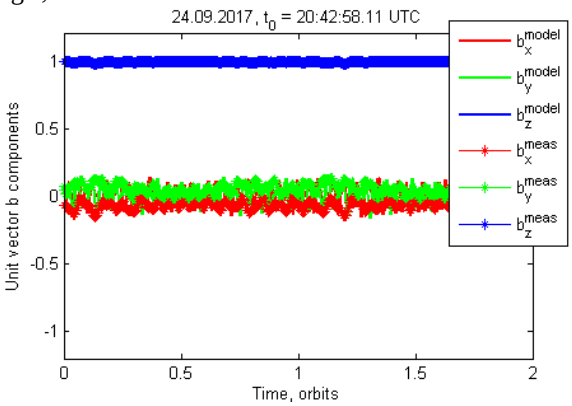

Fig. 18. Measured and predicted unit vector along the geomagnetic field

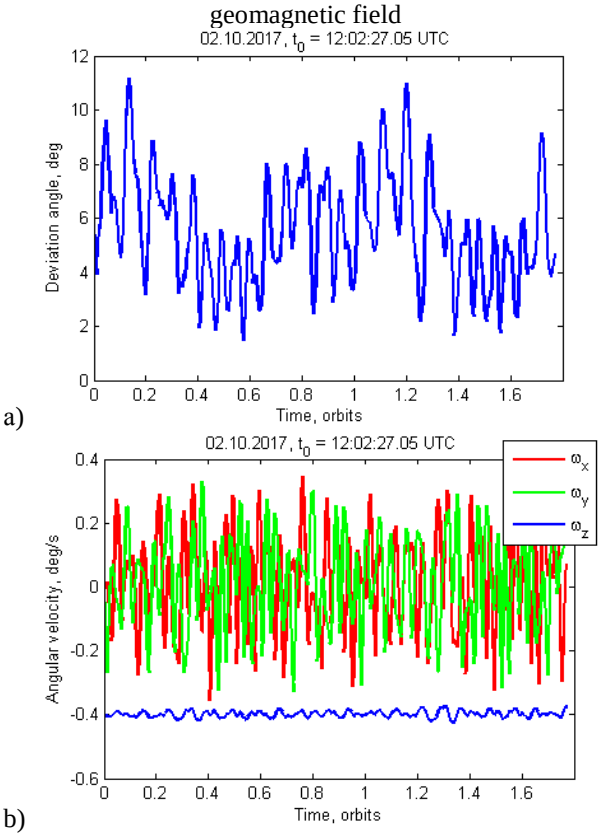

Fig. 19. Angle of deviation of the OZ axis of the satellite from the direction of the local magnetic field (a) and the angular velocity during steady-state motion (b)

Measurements from photodiode sun sensors were predicted based on the initial conditions obtained, and their values were compared with telemetry data. The result of the comparison is shown in Fig. 20. The measurement forecast coincides with some accuracy with the measurements of the photodiode sensors. It should be noted that a cosine-wave sensor measurement model was used for the prediction of measurements, which does not work well at large deviation angles, and the contribution from the Earth's albedo was not taken into account. The 5th and 6th solar sensors are located on the opposite sides of the satellite body. Therefore at the time when the measurements of the 5th sensor are close to unity, the measurements of the 6th sensor reaches 0.3 value, that can be caused only by the reflection of sunlight from the Earth. Thus, the fact is confirmed that the albedo of the Earth can be up to 30% of the solar radiation is confirmed.

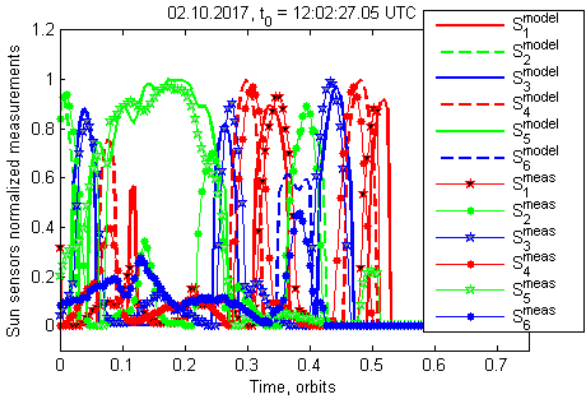

Fig. 20. Sun sensors normalized measurements and its predicted values

4.4 Orbit degradation

Initial ISS orbit on the launch date was about of altitude of 410 km. During the last year the average index of solar activity was about the value of $F_0 = 75 \cdot 10^{-2}$ W/(m^2·Hz) which characterizes very low level of the solar activity. The atmosphere density strongly depends on the solar activity and its values is comparatively low on that altitudes. That is why during the year the satellite altitude decreased only on 30 km. Fig. 7 shows the onboard GPS/GLONASS measurements during one year. Fig. 8 presents an apogee and perigee altitudes based on the TLE-data with interpolation till the end of the 2018 year.

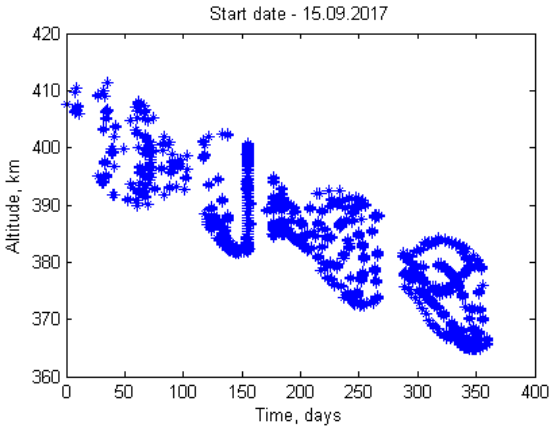

Fig. 21. An altitudes calculated using GPS/GLONASS reciever

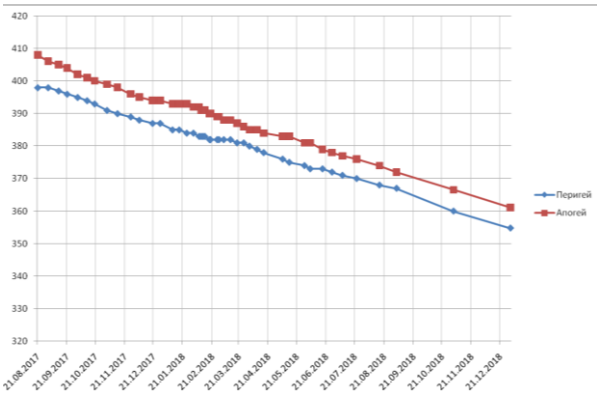

Fig. 22. Apogee and perigee calculated using TLE data and its extrapolation till the end of the 2018 year

4.5 Details on the communication sessions

The TNS-0 #2 satellites upload and download the telemetry and other information via Globalstar antennas installed onboard and via VHF channel. For successful communication session via Globalstar it is necessary the TNS-0 and Globalstar satellites are to be in the line of sight, and at the same time the Globalstar satellite and the Globalstar gateway are also to be in the line of sight. The Globalstar ground stations are shown in Fig. 23.

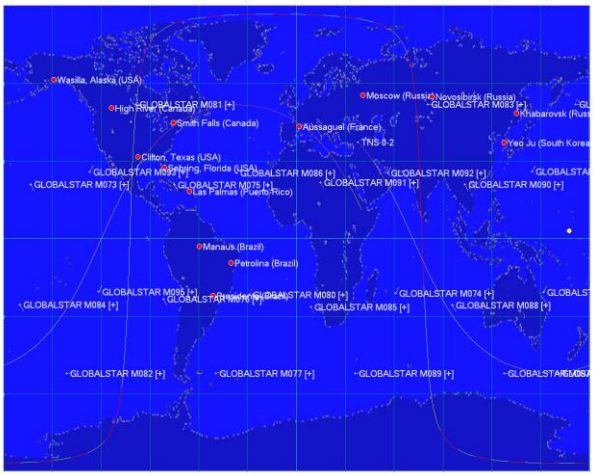

Fig.23. Globalstar ground stations and Globalstar satellites traces

Summary, 1654816 telemetry frames with a total volume of 50 MB were received, 14519 commands were sent to TNS-0 #2 and confirmation of execution was gotten back for 10661 of them.. The size of the TNS-0 #2 telemetry frame is 32 bytes. The table 1 summarize quantity and duration of the communication sessions via Globalstar and VHF channels. The communication session via Globalstar-internet channel is assumed to be successful if at least one telemetry frame is received. If a single SYN-frame is received by the server or the telemetry data is received but remained in the TCP-socket because of broken TCP-sequence, then the communication session is considered as failed. The telemetry can be obtained also via Globalstar-modem channel. If modems have not completed the handshaking procedure, the Globalstar asynchronous session is considered as failed. Finally if ground-based VHF equipment has received at least one telemetry packet with a correct checksum, then the VHF session is considered as successful. Also the communication is failed if the VHF session was scheduled but ground VHF-stations (placed in Moscow and Samara) were not ready.

Table. 1. Communication sessions summary (since 18.08.2017 till 03.09.2018)

Type of session	Successful	Failed	Total	Total duration	Mean duration
Globalstar (internet)	4053	533	4586	95:29:49	0:01:25
Globalstar (modem)	9	34	43	0:25:35	0:02:51
VHF	848	132	982	84:04:04	0:05:57
Total	**4910**	**699**	**5611**	**179:59:28**	**0:02:12**

The number of the communication sessions with certain duration is presented in Table 2. Total duration of communication sessions per month via Globalstar and via the VHF-channel is shown in Fig. 24 and 25.

Table. 2. Number of sessions by duration (all types of sessions)

Duration	Number of sessions
< 1 min	2094
1-2 min	1007
2-3 min	568
3-4 min	292
4-5 min	210
5-6 min	157
6-7 min	164
7-8 min	264
8-9 min	145
9-10 min	7
10 min and longer	4

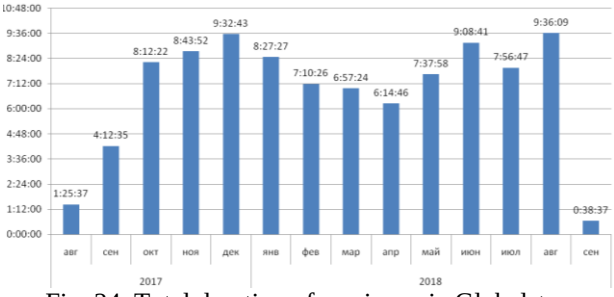

Fig. 24. Total duration of sessions via Globalstar

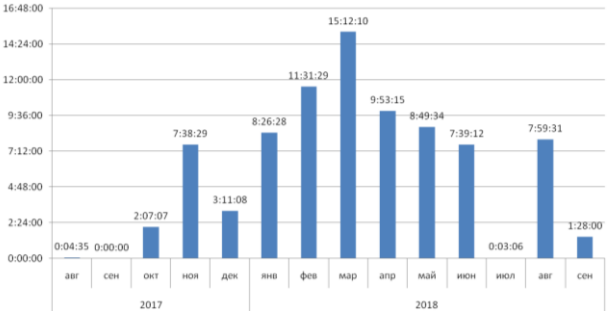

Fig. 25. Total duration of sessions via VHF

In VHF mode the on-board computer transmits a telemetry packet of 2 frames every 2 seconds (1 second is transmission, 1 second is receiving). In the Globalstar-modem mode the on-board computer transmits 2 frames per second.

In the Globalstar-internet mode the satellite transmits packets of 4 frames (128 bytes) every 600 msec. In practice, there are delays in the transmission of data over the Internet (up to 19 seconds between packets) are present as the result of packet loss during transmission through the radio link between the TNS and the Globalstar satellites, which leads to a

retransmition of the data block. This all reduces the average channel capacity.

In VHF mode, a header from the sync sequence (92 bytes) and M-sequence (4 bytes) is added to each transmitting packet. When transferring through the "Globalstar" asynchronous mode, there are no overheads for the transmitting data. When transferring via the Globalstar Internet, TCP and IP headers (27 bytes) are adding to each packet.

Table 3 shows an average channels capacity obtained experimentally and its theoretical values. One can see that actual channel capacity is the best for the Globalstar-internet communication comparing to the other two, but its value is quite far from the theoretical one because of the delays and losses described above. However, the elaboration of on-board algorithms for communication via Globalstar-internet allowed to obtain actual channel capacity up to 420-440 bytes/s, that one can see from the Fig. 26.

Table 3. Mean channels capacity

Mean channel capacity (byte/sec)	**Globalstar-internet**	**Globalstar-modem**	**VHF**
Actual	110-127	64	32
Theoretical	900	900	1200

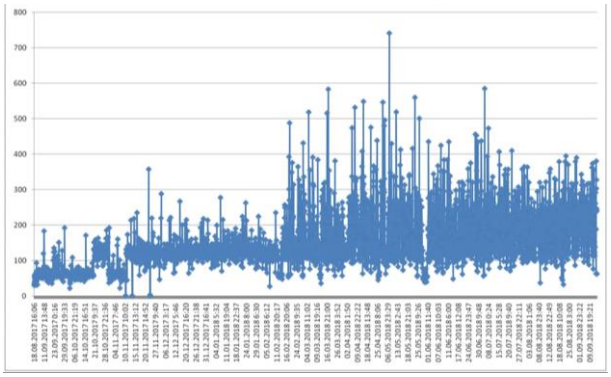

Fig.26. Mean channel capacity Globalstar-internet during the session (bytes/sec)

The total size of the telemetry obtained via Globalstar per month is presented in Fig. 27.

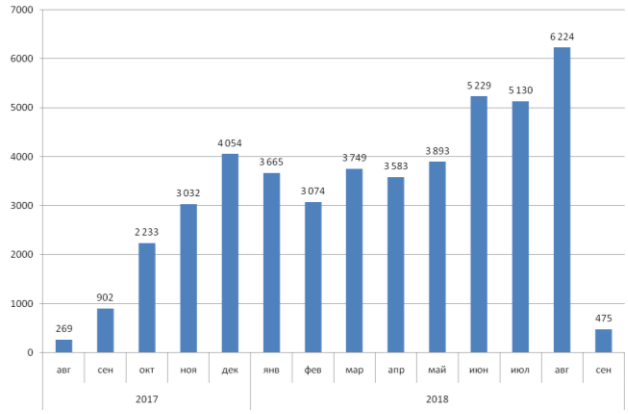

Fig. 27. The total size of the telemetry obtained via Globalstar per month (kB)

Conclusions

Using the telemetry data the angular motion is estimated. Based on this data it is evaluated the damping time which was spent to achieve magnetic attitude when the longitudinal axis of the satellites directed along the local geomagnetic field induction vector. In the steady-state motion, the satellite rotates relative to this direction with an angular velocity of 0.4 deg/s, and the amplitude of oscillations of the longitudinal axis with respect to the magnetic field vector reaches 11 degrees, the oscillation period is about 9 minutes. After one year on orbit the perigee is reduced from 410 km to 380 km. The satellite is communicated via both the Globalstar system and VHF channel. The actual average Globalstar channel capacity of about 430 bytes/s was achieved.

Acknowledgements

The work is supported by Russian Science Foundation, grant 17-71-20117.

References

[1] V.A. Sarychev, M.Y. Ovchinnikov, Satellite Magnetic Attitude Control Systems, Itogi Nauk, VINITI, Moscow, 1985.

[2] V.A. Sarychev, M.Y. Ovchinnikov, Attitude magnetic stabilization using spherical damper, Cosm. Res. 24 (1986) 803–815.

[3] V.A. Sarychev, M.Y. Ovchinnikov, Attitude motion of the satellite with permanent magnet, Cosm. Res. 24 (1986) 527–543.

[4] V.A. Sarychev, V.V. Sazonov, Estimation of the infuence from the eddy-current on the fast satellite rotation, Cosm. Res. 2 (1982) 297–300.

[5] V.A. Sarychev, V.V. Sazonov, Optimal parameters of the passive magnetic attitude control systems, Cosm. Res. 14 (1976) 198–208.

[6] M.L. Battagliere, F. Santoni, M. Ovchinnikov, F. Graziani, Hysteresis rods in the passive magnetic stabilization system for university micro and nanosatellites, in: Proc. 59th IAC, Glas. UK, 29 Sept.

October, Pap. IAC-08.C.1.8, 2008: p. 10.

[7] M. Long, A. Lorenz, G. Rodgers, E. Tapio, G. Tran, K. Jackson, R. Twiggs, T. Bleier, A Cubesat Derived Design for a Unique Academic Research Mission in Earthquake Signature Detection, in: 16th Annu. Conf. Small Satell. Logan, Utah US, 12-15 August, 2002, Pap. SSC02-IX-6, n.d.: p. 17.

[8] Y. Tsuda, N. Sako, T. Eishima, T. Ito, Y. Arikawa, N. Miyamura, A. Tanaka, S. Nakasuka, University of Tokyo's CubeSat Project - Its Educational and Technological Significance, in: 15th Annu. AIAA/USU Conf. Small Satell. Logan, Utah, 13 – 16 August, 2001, Pap. SSC01-VIIIb-7, n.d.: p. 8.

[9] M.L. Battagliere, F. Santoni, F. Piergentili, M. Ovchinnikov, F. Graziani, Passive magnetic attitude stabilization system of the EduSAT microsatellite, Aerosp. Eng. 224 (2010) 1097–1107.

[10] F.T. Hennepe, B.T.C. Zandbergen, R.J. Hamann, Simulation of the Attitude Behaviour and Available Power Profile of the Delfi-C3 Spacecraft with Application of the OpSim Platform, in: Pap. 1st CEAS Eur. Air Sp. Conf. Berlin, Ger. 10-13 Sept. 2007, n.d.: p. 9.

[11] M.Y. Ovchinnikov, D.S. Ivanov, N. a. Ivlev, S.O. Karpenko, D.S. Roldugin, S.S. Tkachev, Development, integrated investigation, laboratory and in-flight testing of Chibis-M microsatellite ADCS, Acta Astronaut. 93 (2014) 23–33. doi:10.1016/j.actaastro.2013.06.030.

[12] D. Ivanov, M. Ovchinnikov, N. Ivlev, S. Karpenko, Analytical study of microsatellite attitude determination algorithms, Acta Astronaut. 116 (2015) 339–348. doi:10.1016/j.actaastro.2015.07.001.

[13] T. Beuselinck, C. Van Bavinchove, V.I. Abrashkin, A.E. Kazakova, V. V. Sazonov, Determination of attitude motion of the Foton M-3 satellite according to the data of onboard measurements of the Earth's magnetic field, Cosm. Res. 48 (2010) 246–259. doi:10.1134/S0010952510030068.

[14] V.I. Abrashkin, K.E. Voronov, Y.Y. Piyakov, V.V. Sazonov, N.D. Semkin, S.Y. Chebukov, Attitude motion of the Photon M-4 satellite, Cosm. Res. 54 (2014) 315–322. doi:10.7868/S0023420616040014.

[15] V.I. Abrashkin, K.E. Voronov, I. V. Piyakov, Y.Y. Puzin, V. V. Sazonov, N.D. Semkin, S.Y. Chebukov, Rotational motion of Foton M-4, Cosm. Res. 54 (2016) 296–302. doi:10.1134/S0010952516040018.

[16] M.Y. Ovchinnikov, V.I. Penkov, D.S. Roldugin, D.S. Ivanov, Magnetic attitude control system for small satellites, KIAM, Moscow, 2016.

[17] S.O. Karpenko, N. V. Kupriyanova, M.Y. Ovchinnikov, V.I. Penkov, A.S. Selivanov, O.E. Khromov, Attitude control system of the first Russian nanosatellite TNS-0 no. 1, Cosm. Res. 48 (2010) 517–525. doi:10.1134/S0010952510060043.

[18] A.P. Kovalenko, Magnetic control systems for spacecrafts, Mashinostroenie, Moscow, 1975.

[19] D.S. Ivanov, M.Y. Ovchinnikov, V.I. Penkov, Laboratory study of magnetic properties of hysteresis rods for attitude control systems of minisatellites, J. Comput. Syst. Sci. Int. 52 (2013) 145–164. doi:10.1134/S1064230712060032.

[20] D.S. Ivanov, M.Y. Ovchinnikov, O.A. Pantsyrnyi, A.S. Selivanov, A.S. Sergeev, I.O. Fedorov, O.E. Khromov, N.A. Yudanov, Nanosatellite TNS-0 №2 Attitude Motion After The Launch From ISS, Cosm. Res. In Press (2018).

[21] V.A. Sarychev, V.I. Penkov, M.Y. Ovchinnikov, Mathematical model of hysteresis based on magneto-mechanical analogy, Math. Simul. 1 (1989) 122–133.

[22] D. Ivanov, M. Ovchinnikov, M. Sakovich, Relative Pose and Inertia Determination of Unknown Satellite Using Monocular Vision, Int. J. Aerosp. Eng. (2018) 1–16. doi:10.1155/2018/9731512.